Self-powered SECE piezoelectric energy harvesting induced by shock excitations for sensor supply

Y.C. Lo, Y.C. Shu *

Institute of Applied Mechanics, National Taiwan University, Taipei 106, Taiwan, ROC

ARTICLE INFO

ABSTRACT

The article studies the piezoelectric frequency up-converted energy harvester endowed with an SP-SECE (self-powered synchronized electric charge extraction) interface circuit. The harvester device comprises a piezoelectric cantilever beam whose tip magnet is impulsively excited by another magnet fixed on a rotating plate. Energy is therefore harvested by resonant vibration of a beam excited at certain discrete driving frequencies. Three aspects are discussed here, including the frequency up-conversion for conditionally resonant power, electrically induced damping for matching impedance and reducing power ripples, and SP-SECE's implementation for power extraction under shock excitations. Precisely, a theoretical model based on the Fourier decomposition of magnetic force is developed for realizing the phenomenon of frequency up-conversion. The SECE electrically induced damping is derived by considering the conversion of energy to electricity in analogy to the dissipation process of a linear mechanical damper. In addition, a novel electronic breaker is implemented for reducing the switching delay effect and enhancing the range of operating voltage. Finally, two experiments are prepared for performance evaluation. The results show the good agreement between the theoretical predictions and the experimental observations. Further, the first one with parameters close to the impedance matching criterion confirms the SECE power outperforms that based on the standard interface. The second one with the SECE electrically induced damping larger than the mechanical damping, the power ripples observed in the SECE case are much more suppressed than that based on the standard interface. Thus, the properties of load-independence and low power fluctuations make the SECE-based frequency up-converted harvester superior in powering sensor nodes operated at around 2–5 volt.

1. Introduction

With the flourish of the data-driven artificial intelligence, the demand of the sensors network for data acquisition is expected to grow nowadays. These sensors are typically powered by electrochemical batteries, giving rise to an issue of an effective power supply as the networks increase in number and the devices decrease in size. Therefore, harnessing energy from sensors' operating environments has received significant attention as a viable alternative solution to batteries. While there are many ambient sources available for power generation, mechanical vibration is a promising potential power source since it is ubiquitous and abundant enough to be of use [1]. In particular, vibrational energy harvesting based on piezoelectric elements has received worldwide research efforts for decades due to various reasons [2]. These incorporate the features of high electromechanical coupling, convenience in scalability, and high voltage output suitable for designing power conditioning circuits. Hence, tremendous progresses

advancing this technology have been reported by numerous researchers from many aspects. These include the theoretical analysis of electromechanical response [3–5] and the conversion efficiency for performance evaluation [6], the harvester designs suitable for energy extraction from various ambient environments [7–9], the search of materials for high electromechanical coupling [10,11], and the energy harvesting circuits for maximum power transfer to the load [12–14].

The aforementioned works are mainly built on resonant vibration, giving rise to the high power at the cost of narrow bandwidth. While there have been various techniques for enlarging the operational bandwidth such as resonance-tuning [15–17], harvester arrays [18–20], multimodal structures [21,22] and the nonlinear harvesters [23–25], the restriction of matching frequency imposed on the dominating frequency spectrum of the excitation sources is still not removed in most of these techniques. Thus, they are not suitable for miniaturized energy harvesters located at the environment with low frequency of motion. Instead, a popular technique for removing such a restriction is based on the mechanism of frequency up-conversion (FUC) [26]. It is capable of transforming low frequency of excitation into high frequency of resonant vibration of the transducer, giving rise to a resonating harvester operated in a non-resonant fashion. Thus, the remaining problem is how the resonance is induced effectively from the smaller-frequency motion of ambient source. This requires different strategies. Typically, the impact [27–29] and plucking [30–32] are the two common approaches for enabling frequency-up. Both have shown unique advantages in specific working environments, but the latter based on magnetic plucking has gained increasing attention due to the creation of contactless energy transfer by reciprocating excitation [26].

In addition to designing suitable harvester structures, the consideration of an interface circuit connecting the piezoelectric element to the terminal load is critical for enhancing power performance. The most popular ones include the standard (STD) interface circuit commonly used for AC/DC conversion [33], the synchronized switching harvesting on an inductor (SSHI) [12] and the synchronized electric charge extraction (SECE) [34] as impedance modifiers. Indeed, the SSHI technique can theoretically achieve the impedance-matching power at the cost of requiring the maximum power point tracking. The SECE circuit exhibits the load-independent property, and therefor, is suitable for low-power-consumption sensors. But the majority of these circuits are designed for harvesters excited harmonically. Few of them is suitable for shock excitations. Indeed, Liu et al. proposed an interface circuit based on a buck–boost converter utilized for replacing the storage capacitor of the standard circuit [35]. They showed the increase of harvested power up to 55% higher than that based on the STD interface operated under a low-frequency vibration environment. Morel et al. presented an SP-SECE (self-powered SECE) circuit suitable for a piezoelectric harvester under shock [36]. They applied the CMOS technology to minimize the electrical power consumption and showed 420% more energy than that based on the STD interface from shock excitations. In addition, Fu et al. combined the beam plucking method and an SSHI circuit for studying piezoelectric energy harvesting [37]. They found the power fluctuations were reduced for plucking harvesters at high frequencies, and extended their approach to the nonlinear oscillator with the property of bi-stability [38].

The article studies the electrical response of an SECE-based piezoelectric energy harvester operated under the reciprocating excitation. Specifically, the tip magnet of a piezoelectric cantilever beam fixed on a stationary base is impulsively plucked by a nearby revolving magnet mounted on a rotating host. Thus, it is an FUC harvester extracted energy from the non-contact magnetic plucking. In comparison with the electromagnetic conversion suitable for less demanding dimensional constraints and high rotating speed cases, piezoelectric transduction combined with FUC mechanism is ideal for small-scale energy harvesters and low-frequency applications [39]. As a result, the latter has shown recent successes in the health monitoring of smart bearings [40], wrist-worn energy harvesting [41,42] and the machine learning-based diagnostics of a timing belt by an SECE energy sensor [43]. Next, from the circuitry point of view, the present type of the FUC harvester has been explored according to various interface circuits, such as AC [32,44], STD [45–47] and SSHI [37] interfaces. Here, the interface SECE is chosen because of the following advantages. First, the electromechanical coupling of a centimeter size of piezoelectric device manufactured by MEMS processing typically is small [48]. Thus, the increase of output power can be realized by nonlinear circuit techniques such as SECE and SSHI. Second, it has been shown that SECE is superior to SSHI in the case of shock excitation [36]. Third, when it comes to resonant operation induced by low frequency of plucking, it typically refers to the excitement of the first resonant mode. But a recent interesting discovery shows the feasibility of inducing different resonant modes simultaneously in an FUC harvester under the two-point magnetic plucking [46]. It raises an issue of different optimal loads for distinct resonant modes. This concern is alleviated due to the low load dependence enjoyed by the SECE strategy. Thus, a need for further investigation of an FUC harvester based on SECE is essential and is studied here.

The article is presented from several perspectives, including the realization of frequency up-conversion, the introduction of electrically induced damping for reducing power fluctuations, and the design of a novel self-powered SECE. The previous two are presented in Section 2 where the analytic expressions of SECE-based power and electrically induced damping ratio are explicitly derived and expressed in terms of system parameters. The circuit design and implementation are presented in Section 3. Note that this issue for realizing the SP-SECE was studied by various works [36,49,50]. Its variants were also proposed in various forms of circuit topologies, such as SP-OSECE (optimized SECE) [51], C-SP-SECE (compact self-powered SECE) [52] and SP-ESECE (efficient SECE) [53]. Most of them were designed based on rectilinear harmonic excitations, giving rise to critical issues regarding to the precise initiation of SECE switching and extremely high peak voltage induced by shock excitation. Indeed, Morel et al. has proposed the logic circuit to achieve the SECE switching control [36]. Their approach allows the realization of the synchronous conditioning circuit on a chip through the CMOS technology at low power overhead. However, the proposed design cannot sustain the piezoelectric voltage higher than 10 volt due to the limitation of the circuit fabrication process. Instead, our beam harvester permits the generation of high peak voltage up to 40 volt due to the magnetic impulsive force acting on the beam tip. Therefore, the electronic-breaker-based circuit design made of discrete circuit components is adopted here for sustaining high peak voltage [54,55]. Its performance on reducing switching delay is improved by the voltage divider design and the MOS-based SECE switch adoption, as detailed in Section 3. Finally, the experimental setup for performance evaluation is presented in Section 4. The results are discussed in Section 5 and the conclusions are made in Section 6.
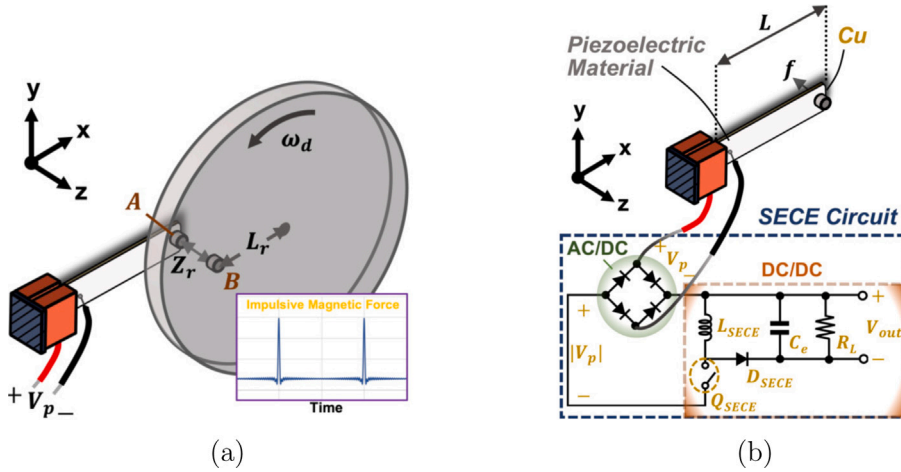
Fig. 1. (a) A piezoelectric cantilever beam is impulsively excited each time when the rotational magnet B from the rotating plate approaches to its tip magnet A. (b) The harvester beam is attached to an SECE interface circuit.

2. Model

2.1. Magnet plucking force and reduced formulation

A piezoelectric cantilever beam is considered and clamped on a stationary base. Its tip magnet A is interacted with another magnet B placed on a circular rotating plate, as shown in Fig. 1(a). It undergoes a stronger impulsive response each time when the rotational magnet B from the rotating plate is approaching to the tip magnet A. The magnetic force acting on the magnet A can be formulated below based on the model of dipole–dipole interaction [45]

$$f(t) = a_m \frac{Z_r(Z_r^2 - \frac{3}{2}d^2)}{(Z_r^2 + d^2)^{\frac{7}{2}}}, \quad d^2 = 2[1 - \cos(w_d t)]L_r^2, \tag{1}$$

where Z_r is the perpendicular distance between the magnets A and B, L_r is the radius of revolution of the magnet B, w_d is the angular driving frequency of the rotating plate and a_m is the coefficient of the magnetic force. According to the study of Shu et al. [45], the force $f(t)$ is shown to be impulsive-like and is much sharper when the ratio $\frac{Z_r}{L_r}$ is getting smaller and smaller, as demonstrated in the bottom right of Fig. 1(a). Due to the periodic excitation by rotary magnetic plucking, the Fourier technique is applied to the impulsive function $f(t)$ for analyzing the phenomenon of frequency up-conversion. Indeed, consider the Fourier cosine expansion of $f(t)$ defined by Eq. (1)

$$f(t) = \sum_n f_n \cos(nw_d t), \quad f_n = \frac{2w_d}{\pi} \int_0^{\frac{\pi}{w_d}} f(t)\cos(nw_d t)dt, \tag{2}$$

where f_n are the Fourier cosine coefficients of $f(t)$. It can be shown that f_n remains non-vanishing for sufficiently larger number of n if the ratio $\frac{Z_r}{L_r}$ is small to make sure $f(t)$ is sharp enough to approximate the Delta function. In addition, Eq. (2) suggests the resonant vibration of the harvester beam could be achieved as long as $nw_d \approx w_{\text{res}}$, where w_{res} is the resonant angular frequency of the piezoelectric beam. The device therefore exhibits the phenomenon of the nth frequency up-conversion transforming the low rotational driving frequency into the high resonant vibration.

Finally, under the circumstance of $w_d \approx \frac{w_{\text{res}}}{n}$ for certain integer n, Shu et al. have shown that the electromechanical response of the device can be described by the following reduced formulations [45]

$$M\ddot{u}(t) + \eta_m\dot{u}(t) + Ku(t) + \Theta V_p(t) = f_n\cos(nw_d t), \tag{3}$$

$$-\Theta\dot{u}(t) + C_p\dot{V}_p(t) = -i_p(t), \tag{4}$$

where $u(t)$ is the displacement of M, $V_p(t)$ the piezoelectric voltage and $i_p(t)$ the current flowing into the specified circuit. In addition, η_m, K, Θ and C_p are the effective mechanical damping coefficient, the stiffness, the piezoelectric coefficient and the capacitance of the piezoelectric beam. Hence, we can imitate the familiar case of a piezoelectric harvester under the rectilinear harmonic excitation to solve the simplified formulations as in Eq. (3) and Eq. (4). Note that Eq. (3) and Eq. (4) are not sufficient to solve three unknowns $u(t), V_p(t)$ and $i_p(t)$. The result depends on what the electronic interface circuit is chosen, as will be described next.
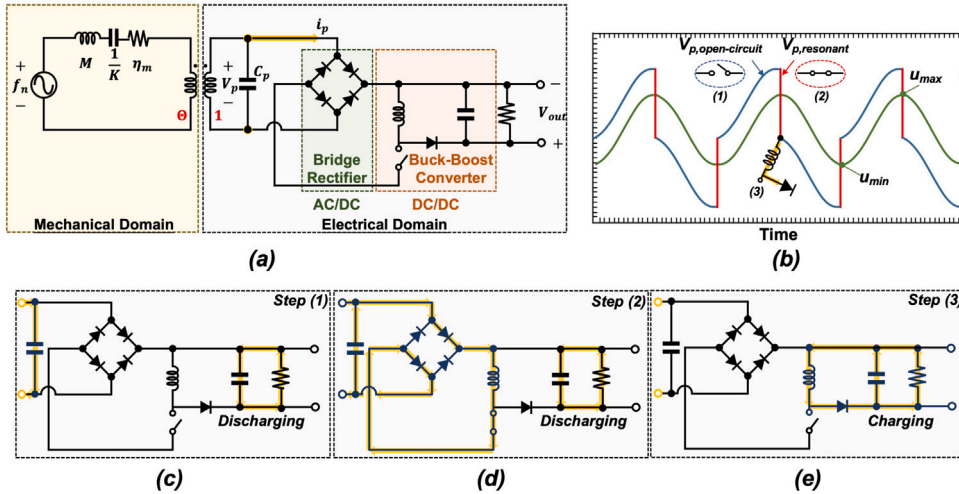
Fig. 2. (a) An equivalent circuit model of a piezoelectric energy harvester attached to an SECE circuit. (b) The waveforms of the piezoelectric voltage and the displacement of the harvester under the SECE conditioning processes. Notice that the SECE operations include three steps: the opening of the switch during the open-circuit excitation (the blue voltage curve in (b) and the yellow current flow in (c)); the close of the switch when the displacement achieves the extreme value (the red voltage curve in (b) and the yellow current flow in (d)); the re-opening of the switch for charge transfer from the inductor to the load (the yellow color in (b) and the yellow current flow in (e)).

2.2. SECE interface circuit

The harvester device is attached to an SECE interface circuit which is suitable for impulsive-like or irregular excitations due to its load-independent property [36,56]. It is schematically shown in Fig. 1(b). Specifically, the SECE circuit is composed of a bridge rectifier to rectify the piezoelectric voltage V_p into $|V_p|$ and a DC/DC converter to rectify the voltage $|V_p|$ into a stable DC voltage V_{out}. In addition, the DC/DC converter is composed of a switch Q_{SECE}, an inductor L_{SECE}, a flyback diode D_{SECE}, a smoothing capacitor C_e and a loading resistance modeled by a resistor R_L.

The operation principle of an SECE circuit is schematically described by Fig. 2(a)-Fig. 2(e) with a brief explanation provided below. First, Eq. (3) and Eq. (4) can be interpreted from the circuitry point of view by introducing an equivalent $R^*L^*C^*$ circuit model shown in Fig. 2(a). The analogy is established by defining several equivalent circuit parameters [18]

$$R^* = \frac{\eta_m}{\Theta^2}, \quad L^* = \frac{M}{\Theta^2}, \quad C^* = \frac{\Theta^2}{K}, \quad V_i^{\text{source}}(t) = \frac{f_n}{\Theta} e^{jnw_d t}, \quad j^2 = -1, \tag{5}$$

as resistor, inductance, capacitance, voltage source and the transformer with ratio $\frac{1}{\Theta}$, respectively. The typical waveforms of $u(t)$ and $V_p(t)$ are schematically shown in Fig. 2(b) where three stages of an SECE conditioning process are presented by different colors. First, the harvester is vibrated under the open-circuit condition, giving rise to the charging on the clamped capacitor C_p with increasing V_p. It is realized by the blue curve shown in Fig. 2(b) and the yellow current flow shown in Fig. 2(c). Second, the SECE switch is conducted whenever the displacement $u(t)$ of the harvester achieves the extreme value. The process is described by the red curve shown in Fig. 2(b) and the yellow current flow from the clamped capacitance C_p to the inductor L_{SECE} as demonstrated in Fig. 2(d). Physically, the energy on the clamped capacitor is transferred to the inductor in this process. Notice that the conduction time is extremely short and the estimate of it is about $\Delta t = \frac{\pi}{2}\sqrt{L_{SECE}C_p}$. This explains the slope of the red line shown in Fig. 2(b) is extremely steep. Finally, the switch is immediately open after one fourth of the period of resonant oscillation with the current flow illustrated by the yellow arrow in Fig. 2(b). As the current in the inductor must be continuous, the current flows through the flyback diode D_{SECE} to charge the load resistance, as shown in Fig. 2(e).

The SECE-based energy harvesting for a single (multiple) piezoelectric oscillator(s) excited under rectilinear excitation has been studied by Tang and Yang [57] (Wu et al. [18]). Based on their result (see Eq. (35) in [57]), the power output derived from Eq. (3) and Eq. (4) can be shown to be

$$P_h^{\text{SECE}} = \frac{2\Theta^2}{\pi C_p}(nw_d) \frac{f_n^2}{\left\{ \left[(nw_d)\eta_m + \frac{4\Theta^2}{\pi C_p} \right]^2 + \left[K - (nw_d)^2 M + \frac{\Theta^2}{C_p} \right]^2 \right\}} \tag{6}$$

for some integer n such that $nw_d \approx w_{\text{res}}$. For the purpose of comparison with the standard (STD) energy harvesting circuit consisting of a full-bridge rectifier followed by a smoothing capacitor for AC/DC conversion, the output power derived by Shu and Lien [33]

is

$$P_h^{\text{STD}} = \frac{(nw_d)^2 \Theta^2 R_L}{\left[\frac{\pi}{2} + (nw_d)C_p R_L\right]^2} \frac{f_n^2}{\left\{\left[(nw_d)\eta_m + \frac{2(nw_d)\Theta^2 R_L}{\left[(nw_d)C_p R_L + \frac{\pi}{2}\right]^2}\right]^2 + \left[K - (nw_d)^2 M + \frac{(nw_d)\Theta^2 R_L}{\left[(nw_d)C_p R + \frac{\pi}{2}\right]^2}\right]^2\right\}}. \tag{7}$$

In contrast to Eq. (7) whose expression shows the dependence on the load R_L, Eq. (6) confirms that the SECE-based power output exhibits the property of load independence.

2.3. Maximum power point and electrically induced damping ratio

A typical feature of a frequency up-converted harvester is the exhibition of ripples characterized by numerous crests and troughs in its power frequency response, as illustrated in Figs. 11 and 12. The crest associated with the nth peak of power evaluated at $w_d = \frac{w_{\text{res}}}{n}$ can be estimated by analyzing the resonant power. The trough viewed as the depth of power fluctuation can be improved by enlarging bandwidth through the induced electrical damping ratio introduced in the second part of this section.

First, the optimal power and its operating points can be obtained by the analysis of impedance matching. The overall impedance Z_m of the mechanical domain shown in Fig. 2(a) can be evaluated by the equivalent circuit model characterized by Eq. (5)

$$Z_m = R^* + j\left(wL^* - \frac{1}{wC^*}\right), \tag{8}$$

where $w = nw_d$. The impedance of the electrical domain depicted in the right side of Fig. 2(a) has been shown to be (see equation (21) in [18])

$$Z_e^{\text{SECE}} = \frac{4}{\pi w C_p} - j\frac{1}{wC_p}. \tag{9}$$

The maximum power and its operating points are therefore realized by

$$P_{\max} = \frac{|V_s|^2}{8\text{Re}[Z_m]}\bigg|_{\text{Re}[Z_m]=\text{Re}[Z_e^{\text{SECE}}], \ \text{Im}[Z_m]=-\text{Im}[Z_e^{\text{SECE}}]}, \tag{10}$$

where $\text{Re}[\cdots]$ and $\text{Im}[\cdots]$ are the real and imaginary parts of the given complex variable. Let the alternative electromechanical coupling factor k_e^2, mechanical damping ratio ζ_m, nondimensional electric resistance r and frequency ratio Ω be defined by

$$k_e^2 = \frac{\Theta^2}{KC_p}, \quad \zeta_m = \frac{\eta_m}{2\sqrt{MK}}, \quad \Omega = \frac{w}{w_{\text{sc}}}, \quad r = C_p R_L w_{\text{sc}}, \tag{11}$$

where $w_{\text{sc}} = \sqrt{\frac{K}{M}}$ is the short-circuit resonant angular frequency. Eq. (10) can therefore be simplified to give the maximum power

$$P_{\max} = \frac{f_n^2}{8\eta_m} \tag{12}$$

evaluated at the matching criterion provided in terms of aforementioned dimensionless parameters

$$\zeta_m = \frac{1}{\Omega}\frac{k_e^2}{\frac{\pi}{2}}, \quad \Omega = \sqrt{1 + k_e^2}. \tag{13}$$

There are two observations drawn from the matching conditions. First, Eq. (13) shows that the criterion is independent of load resistance, as expected. Second, Eq. (13) can be re-examined by introducing the electrically induced damping ratio ζ_e so that the conversion of energy to electricity is similar to the dissipation process experienced by a linear mechanical damper [6]. In other words, the total damping ratio ζ_{tot} of a linear damper is the sum of ζ_m and ζ_e. In addition, the efficiency of mechanical to electrical energy conversion can be defined in terms of the ratio ζ_e to ζ_{tot} by [6]

$$\text{eff} = \frac{W^e}{W^m + W^e} = \frac{\zeta_e}{\zeta_m + \zeta_e}, \tag{14}$$

where W^e and W^m are the time-averaged power dissipated across the electrical load and the power dissipated due to the mechanical damping, respectively. Following the approach proposed by Shu and Lien [6] for the case of the standard interface circuit, the efficiency of the SECE-based system is obtained by

$$\text{eff} = \frac{\frac{1}{2}C_p V_M^2}{\frac{\pi}{2}w\eta_m u_0^2 + \frac{1}{2}C_p V_M^2}, \tag{15}$$

where u_0 is the amplitude of the displacement $u(t)$ and V_M is the magnitude of the piezoelectric voltage V_p on the capacitance C_p when the harvester is harmonically excited under the open-circuit condition. Both are related by $V_M = \frac{2\Theta}{C_p}u_0$ obtained by integrating Eq. (4) over one-half period of excitation under $i_p(t) = 0$ (see equation (9) in [57]). Therefore, Eq. (15) can be written as

$$\text{eff} = \frac{\frac{2}{\pi}\frac{k_e^2}{\Omega}}{\zeta_m + \frac{2}{\pi}\frac{k_e^2}{\Omega}}, \tag{16}$$
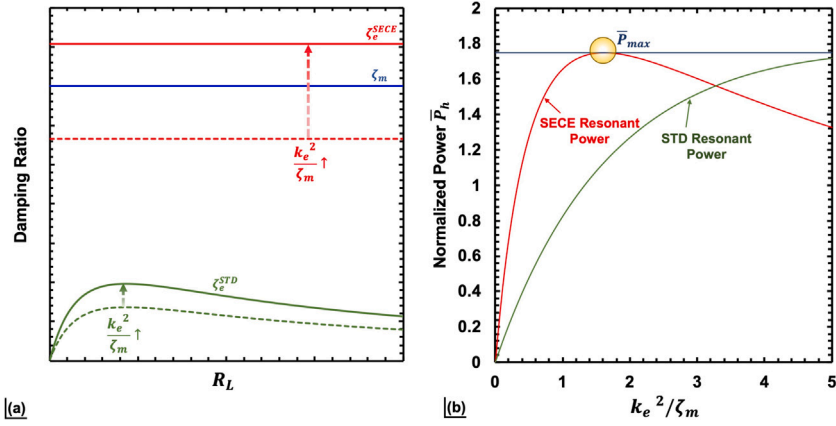
Fig. 3. (a) The electrically induced damping ratio ζ_e is plotted against the load R_L for the SECE (red color) and STD (green color) interface circuits. Both curves will move upward by increasing $\frac{k_e^2}{\zeta_m}$. (b) The resonant power is plotted against $\frac{k_e^2}{\zeta_m}$ for the SECE (red color) and STD (green) interfaces. The horizontal straight blue line represents the upper bound of power when the impedance matching is achieved.
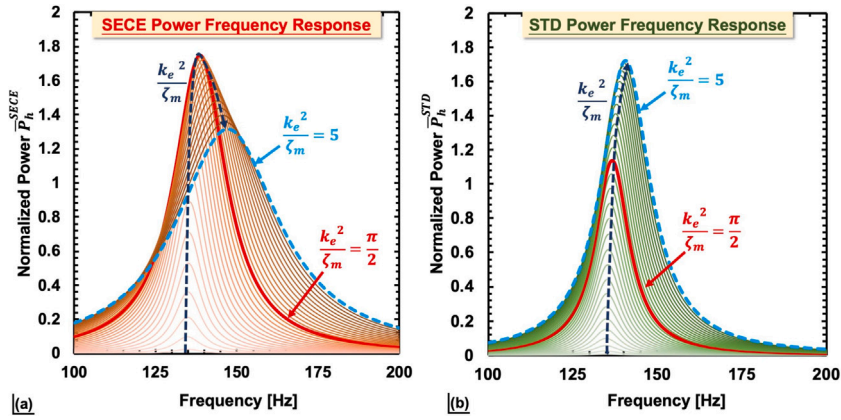
Fig. 4. The power frequency responses are plotted and evaluated under various magnitudes of $\frac{k_e^2}{\zeta_m}$ for the SECE interface as in (a) and the STD interface as in (b), respectively. The thick red curves are those evaluated at $\frac{k_e^2}{\zeta_m} = \frac{\pi}{2}$ and the thick blue dashed curves are those evaluated at $\frac{k_e^2}{\zeta_m} = 5$. Notice that the dark blue dashed curves are the envelopes of the peaks of power.

and the comparison between Eq. (14) and Eq. (16) gives

$$\zeta_e^{\text{SECE}} = \frac{2}{\pi} \frac{k_e^2}{\Omega}. \tag{17}$$

It follows that the criterion for impedance matching in Eq. (13) can be re-formalized to be

$$\zeta_m = \zeta_e^{\text{SECE}} = \frac{2}{\pi} \frac{k_e^2}{\Omega} \quad \text{(SECE impedance criterion)}, \tag{18}$$

operated at the open-circuit resonant angular frequency $w_{\text{oc}} = \sqrt{1 + k_e^2} w_{\text{sc}}$.

For the purpose of comparison, the electrically induced damping ratio ζ_e^{STD} based on the standard (STD) interface circuit is (see equation (21) in [6])

$$\zeta_e^{\text{STD}} = \frac{r k_e^2}{\left(r\Omega + \frac{\pi}{2}\right)^2}. \tag{19}$$

Fig. 3(a) shows the typical plots of the electrically induced damping ratio ζ_e against the load R_L for both SECE and STD interfaces assuming $\Omega \approx 1$ in the case of the weak/medium electromechanical coupling. Obviously, ζ_e^{SECE} is a horizontal straight line in Fig. 3(a) since its expression is independent of load resistance from Eq. (17). In contrast, ζ_e^{STD} shows the strong dependence on the

Table 1

Validation of Eq. (21) describing the relation between the total damping ratio ($\zeta_m + \zeta_e$) with the estimated power bandwidth for the SECE and STD interfaces.

$\frac{k_e^2}{\zeta_m}$	SECE					STD				
	ζ_m	ζ_e^{SECE}	$2(\zeta_m + \zeta_e^{\text{SECE}})$	$\frac{\Delta f}{f_{\text{res}}}$	err	ζ_m	ζ_e^{STD}	$2(\zeta_m + \zeta_e^{\text{STD}})$	$\frac{\Delta f}{f_{\text{res}}}$	err
$\frac{k_e^2}{\zeta_m} = \frac{\pi}{2}$	0.034	0.034	0.136	0.144	5.5%	0.034	0.0085	0.085	0.091	6.5%
$\frac{k_e^2}{\zeta_m} = 5$	0.034	0.117	0.302	0.283	6.7%	0.034	0.031	0.13	0.121	7.4%

load, and its maximum evaluated at $r = \frac{\pi}{2}$ is

$$\max_r \zeta_e^{\text{STD}} = \frac{1}{4} \frac{k_e^2}{\frac{\pi}{2}} = \frac{1}{4} \zeta_e^{\text{SECE}}. \tag{20}$$

Thus, given an energy harvester with fixed k_e^2, ζ_e^{SECE} is at least 4 times larger than ζ_e^{STD}, as schematically illustrated in Fig. 3(a). A consequence of this fact is that the impedance matching is achieved earlier in the SECE case than the STD case when k_e^2 is gradually increased to the value $\frac{\pi}{2}\zeta_m$ to guarantee $\zeta_e^{\text{SECE}} = \zeta_m$, as in Eq. (18). It can also be seen in the yellow circle marked at the peak of the SECE power evaluated at $\frac{k_e^2}{\zeta_m} = \frac{\pi}{2}$ in Fig. 3(b) where the normalized power $\overline{P}_h = \left(\frac{w_{\text{sc}} M}{f_n^2} \right) P_h$ is plotted against the parameter $\frac{k_e^2}{\zeta_m}$ for both SECE and STD cases. When the ratio $\frac{k_e^2}{\zeta_m}$ is increased and greater than $\frac{\pi}{2}$, Fig. 3(a) demonstrates $\zeta_e^{\text{SECE}} > \zeta_m$ and ζ_e^{STD} is also increased from the bottom to approach ζ_m. It results in the reduction of the SECE power and the increase of the STD power, as shown in Fig. 3(b).

Next, the aforementioned discussions are mainly focused on the matching conditions for the optimal power and its variations due to the mismatch between ζ_e and ζ_m. Another key factor for designing FUC harvesters is the reduction of power ripples often seen in the power frequency response. The depth of the power fluctuation can be reduced by requiring a wider bandwidth. A common indicator for estimating the frequency bandwidth is the half-power bandwidth Δf originally proposed by Papagiannopoulos et al. without considering the piezoelectricity and circuitry [58]. Their formulation is employed by assuming the replacement of ζ_m with ζ_{tot}

$$\frac{\Delta f}{f_{\text{res}}} \approx 2\zeta_{\text{tot}} = 2(\zeta_m + \zeta_e), \tag{21}$$

where $f_{\text{res}} (= \frac{1}{2\pi} w_{\text{res}})$ is the resonant frequency of the device. To see how Eq. (21) works for the present situation, consider the normalized power frequency response shown in Fig. 4(a) and Fig. 4(b) for the SECE and STD interfaces, respectively. First, the dark blue dashed curve in Fig. 4 represents the connection of all peaks of power evaluated at various magnitudes of k_e^2. The red and blue curves are those corresponding to different ratios $\frac{k_e^2}{\zeta_m} = \frac{\pi}{2}$ and $\frac{k_e^2}{\zeta_m} = 5$, respectively. The former is the case of $\zeta_e^{\text{SECE}} = \zeta_m$ for impedance matching in the SECE interface, while the latter is an illustration of the case $\zeta_e^{\text{SECE}} > \zeta_m$. Table 1 lists the error of estimating $\frac{\Delta f}{f_{\text{res}}}$ based on the total damping ratio as in Eq. (21) for $\frac{k_e^2}{\zeta_m} = \frac{\pi}{2}$ and 5, respectively. The results are satisfactory as the errors are within the range between 5%–7% for both SECE and STD interface circuits.

A consequence of Eq. (21) is that the size of power ripples in the frequency response can be adjusted through the control of the electrically induced damping ratio ζ_e. Indeed, from Table 1,

$$\left(\frac{\Delta f|_{\frac{k_e^2}{\zeta_m}=5}}{\Delta f|_{\frac{k_e^2}{\zeta_m}=\frac{\pi}{2}}} \right)_{\text{SECE}} = \frac{0.283}{0.144} \approx 200\% > \left(\frac{\Delta f|_{\frac{k_e^2}{\zeta_m}=5}}{\Delta f|_{\frac{k_e^2}{\zeta_m}=\frac{\pi}{2}}} \right)_{\text{STD}} = \frac{0.121}{0.091} \approx 130\%. \tag{22}$$

Therefore, the enlargement of bandwidth by adjusting ζ_e is much more significant in the SECE case than in the STD case at the cost of less amount of power. This theoretical analysis will be used for designing SECE-based frequency up-conversion energy harvester with small power ripples, as described in Section 5.

3. Novel electronic breaker SECE

In the case of rectilinear harmonic periodic excitations, the magnitude of piezoelectric voltage across the piezoelectric element remains fixed as illustrated in Fig. 2(b). However, it is not fixed and is continuously damped under shock excitations, as in the present case under the rotary magnetic plucking. Thus, the time intervals within two adjacent peak voltages are not uniform, causing the difficulty in implementing the SECE technique. It therefore requires a new controller circuit for initiating the switching events. Here, a novel electronic breaker (NEB) is proposed for controlling a buck–boost converter operated under the discontinuous conduction mode for DC to DC rectification. Its control topology is shown in Fig. 5(a) whose function can be described by 4 control blocks named A, B, C and D as shown in Fig. 5(b). Specifically, the blocks A and B comprise the RC filter and another two blocks C and D comprise two ideal switches for controlling the SECE switch marked by the yellow color in Fig. 5. The operations of the proposed novel electronic breaker can be classified into three steps schematically illustrated in Fig. 5(c)-Fig. 5(e) where the flow of the current
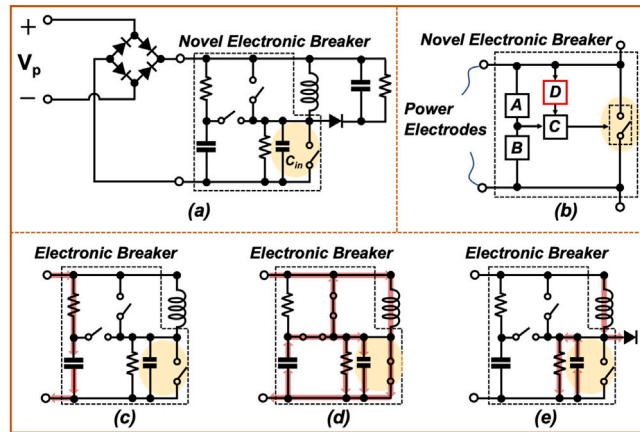
Fig. 5. (a) The topology of the proposed self-powered SECE circuit. (b) Schematic of the novel electronic breaker which consists of four control blocks, denoted by A, B, C and D. Its operation is classified into three steps: the open-circuit state as in (c), the resonant state as in (d) and the charging state as in (e).
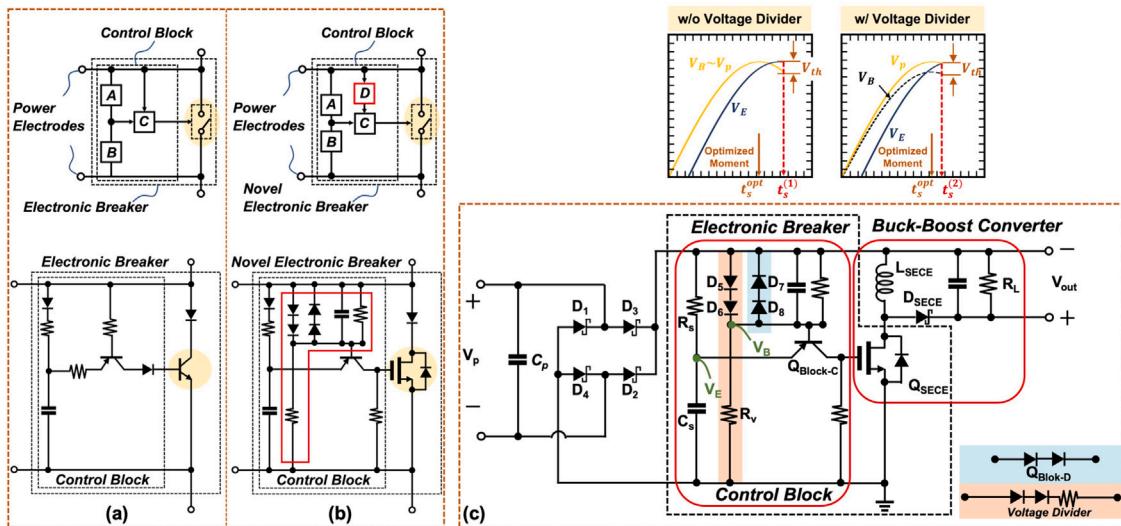
Fig. 6. (a) Schematic of a conventional electronic breaker. (b) Schematic of the novel electronic breaker (NEB) with MOS switch replacement and a new control block D. (c) The circuit schematic of the self-powered NEB-SECE.

is marked by red color arrows. First, when the piezoelectric oscillator is excited at the open-circuit condition to boost the voltage as demonstrated by the blue curve in Fig. 2(b), Fig. 5(c) shows that three switches are open and the RC filter is charged. Next, when the piezoelectric voltage reaches the extreme value, Fig. 5(d) indicates that all of the switches are activated by the energy previously accumulated on the capacitor in the RC filter. This corresponds to the second stage marked by the red curve in Fig. 2(b), and the energy on the piezoelectric clamped capacitance is converted to the inductor by the LC oscillation. Finally, Fig. 5(e) shows that the charge on the input capacitor is recovered to zero for disconnecting the SECE switch again. As a result, the inductor charge is transferred to the load resistance as also illustrated in the third stage of Fig. 2(b).

Before the specific description of implementing NEB in SECE, it is noted the electronic breaker switching method applied to nonlinear energy harvesting interfaces was originally proposed by Lallart and Guyomar [13]. Fig. 6(a) is an illustration of their proposed electronic breaker circuit which has been shown to be efficient in charging control for self-powered vibration harvesters. However, there are two drawbacks in the original design of the electronic breaker circuit. First, the BJT switch shown in the bottom of Fig. 6(a) exhibits the larger switch resistance than the MOS switch during conduction. In addition, the traditional electronic breaker exhibits the switching delay to conquer the threshold voltage of the BJT switch in the control block C shown in Fig. 6(a). To overcome these two disadvantages, the MOS switch is adopted to replace the BJT switch. But the direct replacement raises an issue since the gate current of the MOS switch is zero. Thus, a new control block D schematically shown on the top of Fig. 6(b) is required to make the current flow out of the capacitor in the RC filter for recovering its charge to be zero. It consists of a voltage divider in parallel with a switch realized by two diodes in series, and is shown in the bottom of Fig. 6(b) to compensate the threshold voltage
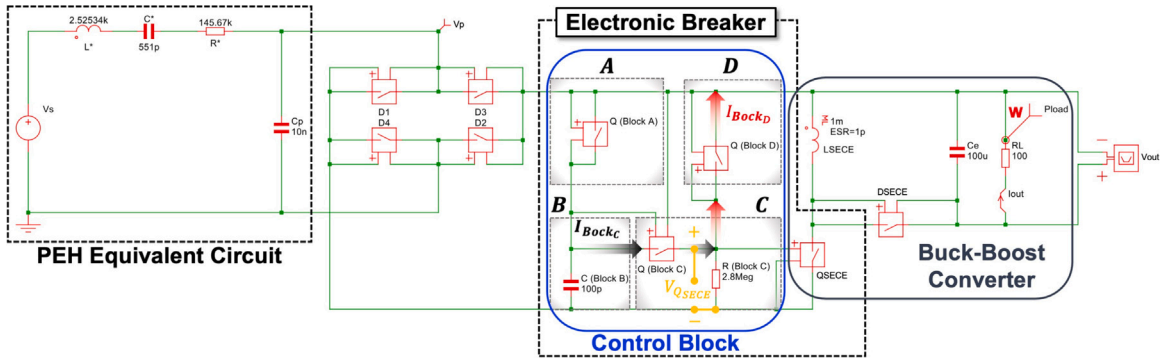
Fig. 7. The circuit schematic of the novel electronic breaker used for SIMetrix simulations. The piezoelectric energy harvester (PEH) is described by an equivalent circuit model established as in Eq. (5). The control box contains all of the constituents required for building the blocks A, B, C and D in Fig. 5(b).

of the switch in block C [59]. The complete circuit schematic of the proposed NEB-SECE is presented in Fig. 6(c). It is fabricated by several discrete circuit components. Specifically, the bridge rectifier is composed of Schottky diodes D_1 - D_4 (BAT48 model) with a forward voltage of 0.2 volt. Two rectifier diodes D_5 - D_8 (1N4004 model) and 10 MΩ carbon composition resistors are selected to comprise the voltage divider. The $Q_{\text{Block}-C}$ and Q_{SECE} are implemented by the PNP silicon transistor (BD136 model) and the small signal NMOS (BS170 model), respectively.

The operation of the new control block D shown in the middle of Fig. 6(c) is briefly analyzed here. First, the voltage divider shown in the orange rectangle of Fig. 6(c) is used for minimizing the switching delay effect. Indeed, at the disconnection of the SECE switch during the open-circuit excitation, the sensing capacitance C_s is charged for detecting the piezoelectric voltage $V_p(t)$. The detection circuit consists of the resistance R_s and the sensing capacitance C_s and is also shown in the control block of Fig. 6(c). It is viewed as a low pass filter so that the sensing voltage V_E is expressed as

$$V_E(t) = \bar{V}_p \frac{\cos\left[wt - \tan^{-1}(R_s C_s w)\right]}{\sqrt{(R_s C_s w)^2 + 1}}, \tag{23}$$

where $\bar{V}_p$ is the magnitude of $V_p(t)$ substituted by a small voltage gap across the bridge diodes and w is the vibration angular frequency. The voltage divider shown in the orange rectangle of Fig. 6(c) is modeled as two diodes with resistance R_D in series with a large resistor R_v. According to the voltage divider rule, the voltage V_B across the diodes D_5 and D_6 is

$$V_B(t) = \bar{V}_p \frac{R_v \cos(wt)}{R_v + 2R_D}. \tag{24}$$

Next, the BJT switch denoted by $Q_{\text{Block}-C}$ is implemented for activating the SECE switch according to the conduction criterion by

$$V_{EB} = V_E - V_B = \bar{V}_p \left\{ \frac{\cos\left[wt - \tan^{-1}(R_s C_s w)\right]}{\sqrt{(R_s C_s w)^2 + 1}} - \frac{R_v \cos(wt)}{R_v + 2R_D} \right\} \geq V_{\text{th}}, \tag{25}$$

where V_{th} is the threshold voltage of the BJT. Let t_s^{opt} be the optimal time instant for activating the SECE switch. It typically corresponds to the peaks of $V_p(t)$. In the original design of the electronic breaker without the voltage divider, the switching instant denoted by $t_s^{(1)}$ is determined by Eq. (25) ($R_D = 0$) and is shown in the top left of Fig. 6(c). Clearly, the phase delay ($t_s^{(1)} - t_s^{\text{opt}}$) is unavoidable. Thanks to the inclusion of voltage divider, the switching instant denoted by $t_s^{(2)}$ can be determined by Eq. (25) ($R_D \neq 0$) and is shown in the top right of Fig. 6(c). As the waveform of V_B with voltage divider is lower than that of V_p, the phase delay ($t_s^{(2)} - t_s^{\text{opt}}$) is smaller than ($t_s^{(1)} - t_s^{\text{opt}}$). It can also be explained graphically by comparing the two figures on the top of Fig. 6(c). Hence, the inclusion of voltage divider is capable of compensating the threshold voltage of the SECE switch for improving the switching phase delay effect. The next issue is the guarantee of disconnecting the SECE switch at the time instant when the piezoelectric voltage V_p is just discharged to vanish. Here, the $Q_{\text{Block}-D}$ composed of two diodes in series and shown in the blue rectangle of Fig. 6(c) is implemented for recovering the energy on the capacitor. Indeed, the Q_{SECE} switch is turned off when the voltage V_E is smaller than the threshold voltage $\bar{V}_{\text{th}}$ of the Q_{SECE} switch. During the conduction period, $V_E = \bar{V}_p + V_D + V_{EB}$ where V_D is the voltage gap across the diodes D_7 and D_8 in series and $V_{EB} = V_{\text{th}}$ as in Eq. (25). Therefore, the Q_{SECE} switch is open when

$$\bar{V}_p + V_D + V_{EB} < \bar{V}_{\text{th}}. \tag{26}$$

From Eq. (26), the switch will be turned off in advanced when $\bar{V}_p = \bar{V}_{\text{th}} - V_{EB} \neq 0$ without the inclusion of $Q_{\text{Block}-D}$ ($V_D = 0$). Therefore, a sufficient number of diodes in $Q_{\text{Block}-D}$ are required so that $V_D = \bar{V}_{\text{th}} - V_{EB}$ to guarantee the vanishing of $\bar{V}_p$ at the instant of switch reopening.

Finally, the validation of the proposed electronic breaker schematically presented in Fig. 5 is numerically carried out by the SIMetrix circuit solver whose circuit schematic is shown in Fig. 7. The piezoelectric device is modeled by an equivalent circuit so that the parameters M, η_m, K and the transformer with ratio $\frac{1}{\Theta}$ presented in Fig. 2(a) are transformed to several equivalent
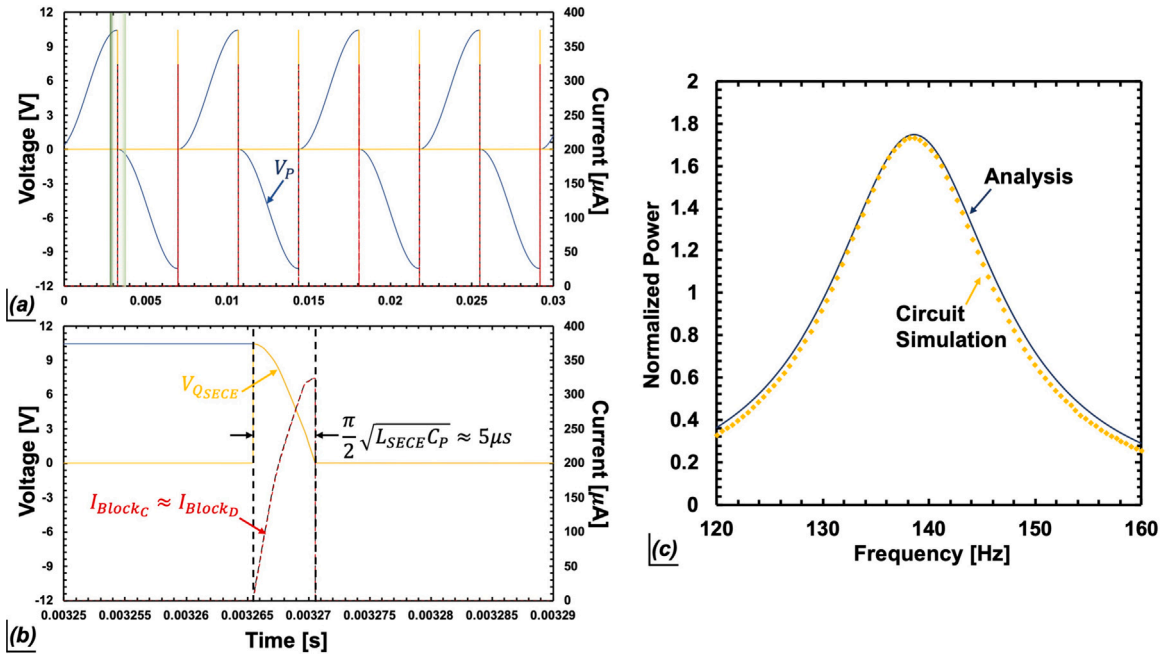
Fig. 8. (a) The time waveforms of V_p (blue), $V_{Q_{SECE}}$ (yellow), I_{Block_C} (black) and I_{Block_D} (red) derived from the SIMetrix simulation. (b) The green region shown in (a) is zoomed in to present the waveforms within the short time of switching ($\sim \frac{\pi}{2}\sqrt{L_{SECE}C_p} \approx 5$ µs). (c) The comparison of the SECE power frequency response between the SIMetrix simulation (yellow) and the prediction (blue) based on Eq. (6).

circuit parameters denoted by R^*, L^* and C^* as in Eq. (5). The values of these parameters used in the SIMetrix simulation are listed in Table 3 drawn from the experiment described in Section 4. In comparison with the proposed electronic breaker shown in Fig. 6, there are several assumptions made in Fig. 7. First, the diodes in the bridge rectifier are implemented by four ideal switches. Second, the resistor in block A is replaced with an ideal switch to avoid the electrical power loss. Third, the switches presented by Q (Block C) and Q (Block D) are also taken to be ideal, and their threshold voltage is set to be close to zero. Finally, the input capacitor of the SECE switch is set to be zero in the simulation of the ideal condition. Fig. 8(a) presents the simulation of the time waveforms of V_p (blue), $V_{Q_{SECE}}$ (yellow), I_{Block_C} (black) and I_{Block_D} (red). The latter three describe the activation processes of the switches Q_{SECE}, Q (Block C) and Q (Block D) marked in Fig. 7. As the duration of switching is extremely short and is in the order of $\frac{\pi}{2}\sqrt{L_{SECE}C_p} \approx 5\mu$ sec, the switching event marked in the green block of Fig. 8(a) is zoomed in and presented in Fig. 8(b). It is found that the switching is initiated immediately after the piezoelectric voltage V_p reaches the extreme value, and the current I_{Block_C} flows through the resistor in the block C to conduct the SECE switch. In addition, as I_{Block_C} is almost equal to I_{Block_D} within the period of switching, the energy accumulated on the capacitor in the block B is almost recovered from the block B to D, and is finally transferred to the inductor L_{SECE}. It is clear from the circuit simulation shown in Fig. 8(b), the operation of the new electronic breaker implemented in SECE is consistent with that described in Fig. 5(d). Finally, the overall power frequency response of the proposed self-powered SECE is simulated and shown in Fig. 8(c). It is found in good agreement with the analytic estimate provided by Eq. (6) with $n = 1$ therein.

4. Experiment

The performance of the proposed harvester device enhanced by the self-powered SECE technique is experimentally evaluated here. Fig. 9 shows the experimental setup consisting of a piezoelectric cantilever beam with a tip magnet impulsively excited by another rotating magnet. Precisely, the bimorph beam, made by Eleceram Technology, contains a Cu substrate whose top and bottom surfaces are paved by two piezoelectric layers. Its sizes in dimensions are $40 \times 10 \times 0.1$ mm^3 for the Cu substrate and $40 \times 10 \times 0.2$ mm^3 for each piezoelectric layer. The tip magnet is impulsively plucked by a magnet attached on a rotating plate driven by a motor (Orientalmotor BLM6200SP-GFV) and the controller (Orientalmotor BMUD200-A). In addition, the self-powered SECE interface with the novel electronic breaker circuit is attached to the harvester beam. The standard interface circuit is also used for the purpose of comparison. The piezoelectric voltage V_p and the output DC voltage V_{out} across the load R_L controlled by the resistance substitution box (IET, RS 201) are measured for various rotational driving frequencies f_d. Finally, all of the measurement data are recorded through the DAQ device (NI 9229).

From Fig. 3, the performance of the SECE technique applied to the piezoelectric energy harvesting is critically influenced by the ratio of electromechanical coupling factor k_e^2 to mechanical damping ratio ζ_m. To perform the parametric studies, two different experimental setups are prepared for creating different values of $\frac{k_e^2}{\zeta_m}$. The idea is inspired by the concept of Rayleigh damping: the
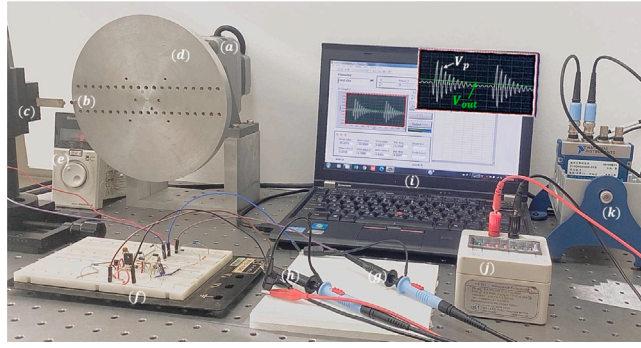
Fig. 9. Experimental setup: (a) motor, (b) magnet *B*, (c) a piezoelectric bimorph clamped by a fixture, (d) rotating plate, (e) motor controller, (f) NEB-SECE circuit, (g) probe for the V_{out} measurement, (h) probe for the V_p measurement, (i) laptop installed with LabVIEW for the voltage measurement, (j) resistance substitution box, (k) DAQ for data acquisition.

Table 2
Fourier cosine coefficients f_n ($\times 10^{-2}$) of the magnetic force $f(t)$ applied to the first and second harvester devices.

	n	10	11	12	13	14	15	16	17	18	19	20
1st	f_n	1.329	1.326	1.316	1.3	1.28	1.254	1.224	1.189	1.152	1.112	1.07
2nd	f_n	1.074	1.083	1.089	1.094	1.097	1.097	1.094	1.09	1.083	1.073	1.062

Table 3
Equivalent parameters of the first and second harvester devices.

	M (g)	η_m (N s/m)	*K* (N/m)	Θ (N/V)	C_p (nF)	k_e	ζ_m	$\frac{k_e^2}{\zeta_m}$	f_{sc} (Hz)
1st	1.09	0.063	785.8	6.6×10^{-4}	10.0	0.235	0.034	1.62	135.1
2nd	0.43	0.0255	679.0	6.07×10^{-4}	10.0	0.233	0.0236	2.31	200

magnitude of mechanical damping ratio ζ_m is enlarged as the mass of the device is increased. Thus, the first setup contains a larger tip magnet on the piezoelectric beam for inducing the higher mechanical damping. The tip magnet is plucked by another magnet on a rotating plate with the radius of revolution $L_r = 70.5$ mm and the perpendicular distance $Z_r = 9.45$ mm. These notations are schematically explained in Fig. 1. From these data, the magnetic interaction force $f(t)$ characterized by the coefficient a_m in Eq. (1) can be realized by matching the theoretical prediction, as in Eq. (1), to the experimental observations (see Fig. 5 in [45]). In the present setup, $a_m = 3.3 \times 10^{-9}$ N m^4. With it, the Fourier cosine coefficients f_n defined by Eq. (2) are listed in Table 2 starting from $n = 10$ to 20. In addition, the equivalent parameters measured at the resonant mode ($n = 11$) are identified based on the standard modal testing, and they are listed in Table 3.

The second setup requires a smaller mechanical damping ratio for increasing the magnitude of the parameter $\frac{k_e^2}{\zeta_m}$. It can be realized by including a smaller magnet on the tip of the beam in comparison to the previous case. In addition, the radius of revolution L_r is 70.5 mm and the perpendicular distance $Z_r = 6.46$ mm, as schematically presented in Fig. 1. The magnetic force coefficient of this second setup is $a_m = 0.87 \times 10^{-9}$ N m^4. With a_m required, the Fourier cosine coefficients f_n defined by Eq. (2) are listed in Table 2 too. Finally, the equivalent parameters measured at the resonant mode ($n = 16$) are identified and are also listed in Table 3.

5. Results and discussions

5.1. Performance of novel electronic breaker SP-SECE

The performance of the proposed novel electronic breaker SP-SECE is experimentally evaluated here, including the pulse response, the operating range and the circuit efficiency under low frequency shock excitations. For illustration, consider the waveform of the piezoelectric voltage V_p shown in Fig. 10. This example is drawn from the aforementioned first experimental setup operated at around the driving frequency $f_d = 5.7$ Hz of the rotating plate. Fig. 10 shows the peak of the pulse response of V_p is about 40 volt immediately after the initial impulsive excitation. It is gradually damped to a vanishing value until the next plucking. Let n be the number of voltage oscillations within the period of free vibration of the harvester. It is observed to be $n = 24$ in the case shown in Fig. 10.

Fig. 10 also reveals that the proposed novel electronic breaker circuit is accurately activated with sufficiently precise switch timing control. But it exhibits the phase delay when the peak piezoelectric voltage is damped to be smaller than 5 volt. This phenomenon can be improved by tuning the resistor values in the envelope detector and in the voltage divider, respectively [59]. Further, there are no charges allowed to be transferred to the load R_L whenever the peak voltage V_p does not exceed the threshold voltage (3.8 volt) of the MOS switch. Thus, from Fig. 10, the number m of the effective oscillations can be defined to be the largest one such that the switching is not allowed in the next adjacent oscillation. In the present case shown in Fig. 10, $m = 10$.
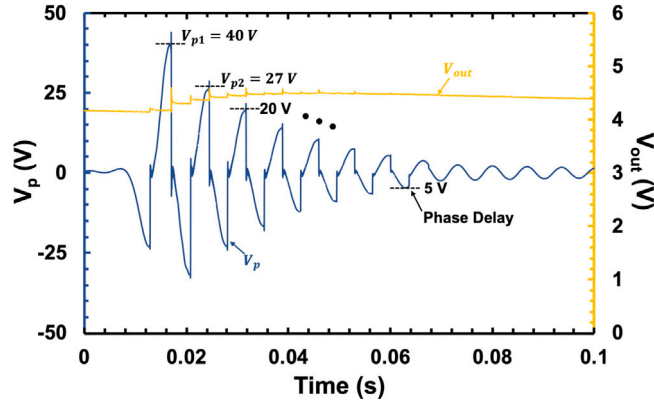
Fig. 10. The waveforms of the piezoelectric voltage (blue) and the output DC voltage (yellow) are measured under the shock excitation of 5.7 Hz. Each peak voltage is measured for estimating the efficiency of the proposed SECE interface circuit.

Finally, the circuit efficiency is defined to be the ratio of the output power to the input power by

$$\text{eff}^{\text{SECE}} = \frac{P_{\text{out}}}{P_{\text{in}}},$$

$$P_{\text{in}} = \left(\sum_i \frac{1}{2} C_p V_{p_i}^2\right) \times f_d, \quad P_{\text{out}} = P_{\text{h}} = \frac{V_{out}^2}{R_L},$$

(27)

where V_{p_i} is the ith peak voltage which is large enough allowing the switching process within the period of plucking excitation. Eq. (27) can be viewed as the efficiency allowing the energy converted from the piezoelectric capacitor to the load resistance. In the case shown by Fig. 10, the circuit efficiency is measured to be around 81% under $f_d = 5.7$ Hz impulsive excitation, $V_{out} = 4.4$ volt and $R_L = 150$ kΩ. In addition, the power consumption of the proposed novel electronic breaker control circuit is around 3.6 μW. Hence, this portion only accounts for 2.8% of the total harvested power P_h.

5.2. Rotary power frequency response

There are two experiments described in Section 4 for evaluating the effect of different $\frac{k_e^2}{\zeta_m}$ on the rotary power frequency response under shock excitations. Consider the first case with $\frac{k_e^2}{\zeta_m}$ being equal to 1.62. Other relevant parameters describing the effective properties of the harvester device are listed in the first row of Table 3. The rotary frequency response of harvested SECE power evaluated at the load 150 kΩ is measured and shown in Fig. 11(a) by red color points. It consists of lots of ripples as the consequence of resonant vibration induced by rotary magnetic plucking. Indeed, the peaks of them correspond to the discrete driving frequencies f_d near $\frac{1}{n} f_{\text{res}}$ for certain integer n, giving rise to the nth frequency up-conversion. The number n can be estimated as follows. From Table 3, the short-circuit resonant frequency $f_{\text{sc}}^{(1)}$ of the first setup is 135.1 Hz. Therefore, the first ripple pair of crest and trough shown in Fig. 11(a) is labeled by $n = 11$ for the driving frequency operated at around 12 Hz. In addition to the crests of ripples, the troughs of ripples are the intersections of two adjacent power curves. The lower of them indicates the pronounced power reduction in the off-resonance region between $\frac{f_{\text{res}}}{n}$ and $\frac{f_{\text{res}}}{n+1}$, and should be avoided in the practical design.

Next, the power prediction based on Eq. (6) for the driving angular frequency $w_d \approx \frac{1}{n} w_{\text{res}}$ (or $f_d \approx \frac{1}{n} f_{\text{res}}$) is also shown in Fig. 11(a) presented by various blue curves starting from $n = 11, 12, 13, \dots$. Obviously, the prediction of crests and troughs of ripples shown in Fig. 11(a) agrees quite well with the experimental observations, giving rise to the soundness of the proposed model presented in Section 2. Notice that Eq. (6) is analyzed based on the circuit loss-free assumption. Thus, for the purpose of fair comparison between the prediction and experiment as presented in Fig. 11(a), various power dissipations during the SECE conditioning process are considered and excluded in Eq. (6). These circuit losses include the power dissipations due to voltage gaps in the full-bridge rectifier and the flyback diode in the converter, and the conversion efficiency between the energy stored in piezoelectric capacitor and that partially transferred to the inductor. The formulations estimating these losses are provided by (A1)-(A5) in the work by Wu et al. [18] under the condition of rectilinear harmonic excitations (see [60] too). Therefore, certain modifications are required for being applied to the case of impulsive excitations. For example, the power dissipated due to the flyback diode is slightly modified by

$$P_{\text{d, flyback}} = \left(\Delta V_{\text{flyback}} \times \frac{V_{out}}{R_L}\right) \times \frac{m}{n},$$

(28)

where $\Delta V_{\text{flyback}}$ is the voltage gap in the flyback diode, n and m have been introduced in Section 5.1: n is the number of free oscillations within a period of adjacent magnetic plucking, and m is the largest number of free oscillations such that the peak of piezoelectric voltage exceeds the threshold voltage of the MOS switch. For instance, $n = 24$ and $m = 10$ are observed in Fig. 10.
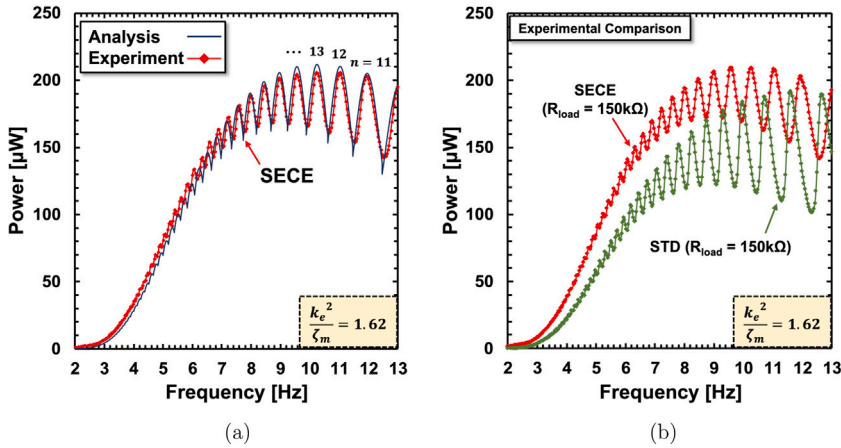
Fig. 11. (a) The rotary SECE power frequency response of the harvester with $\frac{k_e^2}{\zeta_m} = 1.62$ is measured and presented by red color points. It is compared with the analytic estimate (blue color) sequentially starting from $n = 11$ in Eq. (6). (b) The measured SECE power (red color) against the driving frequency is compared with the STD power (green color) evaluated at around the optimal load.
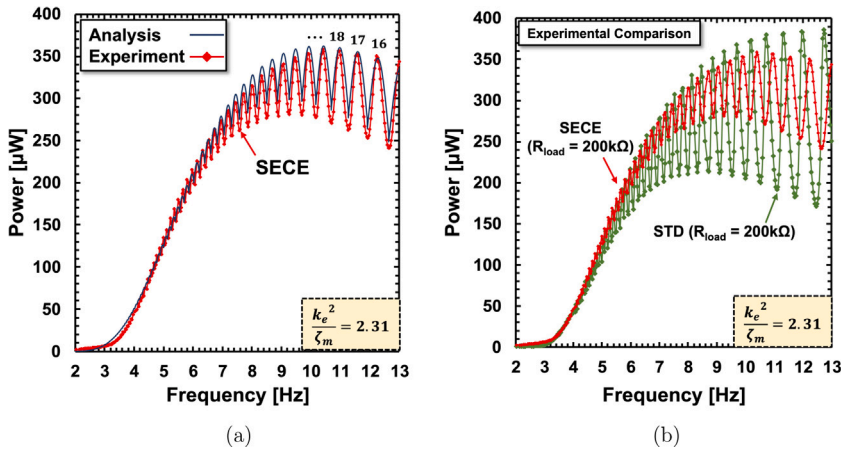
Fig. 12. (a) The rotary SECE power frequency response of the harvester with $\frac{k_e^2}{\zeta_m} = 2.31$ is measured and presented by red color points. It is compared with the analytic estimate (blue color) sequentially starting from $n = 16$ in Eq. (6). (b) The measured SECE power (red color) against the driving frequency is compared with the STD power (green color) evaluated at around the optimal load.

Fig. 11(b) makes a comparison of the rotary power frequency between that based on the SECE (red color) and the STD (green) interface circuits. Two observations are drawn from Fig. 11(b). First, the peaks of SECE power are higher than STD power as the parameter $\frac{k_e^2}{\zeta_m} = 1.62$ is close to the condition of impedance matching requiring $\frac{k_e^2}{\zeta_m} = \frac{\pi}{2}$ suggested by Fig. 3(b). Second, the size of ripples (crests subtracted by troughs) of the SECE case are observed to be much smaller than the STD case. This can be explained by employing the electrically induced damping ratio as schematically depicted by Fig. 4. Indeed, from Eq. (17), Eq. (19) and the parameters listed in the first row of Table 3, ζ_e^{SECE} is 0.034 and ζ_e^{STD} is 0.008, giving rise to the enlargement of bandwidth. The consequence of it is the significant reduction of power fluctuations in the frequency response of the SECE case shown in Fig. 11(b).

We now discuss the experimental results drawn from the second experimental setup whose harvester device exhibits a smaller mechanical damping ratio, giving rise to larger $\frac{k_e^2}{\zeta_m} = 2.31$, as listed in the second row of Table 3. Fig. 12(a) is the rotary power frequency response based on the SECE interface circuit (red color points). Similar to the previous case, each ripple pair of crest and trough is the result of resonant vibration induced whenever the driving frequencies f_d are close to the resonant frequency f_{res} divided by certain integer n. For example, from the second row of Table 3, the short-circuit resonant frequency $f_{\text{sc}}^{(2)}$ is around 200 Hz. Therefore, the driving frequency resulting in the first ripple pair labeled by $n = 16$ in Fig. 12(a) is operated at around 12.4 Hz. Further, the SECE power output predicted by Eq. (6) is evaluated and presented by various blue curves indexing by $n = 16, 17, 18, \ldots$ in Fig. 12(a) too. Obviously, the theoretical predictions are found in good agreement with the experimental observations.

Fig. 12(b) is the experimental comparison of rotary power frequency response between that based on the SECE interface and that based on the STD interface. Different from the previous case, the peaks of the SECE power output are slightly smaller than those of the STD power due to two reasons. First, the criterion of impedance matching for SECE, as described in Section 2.3, requires
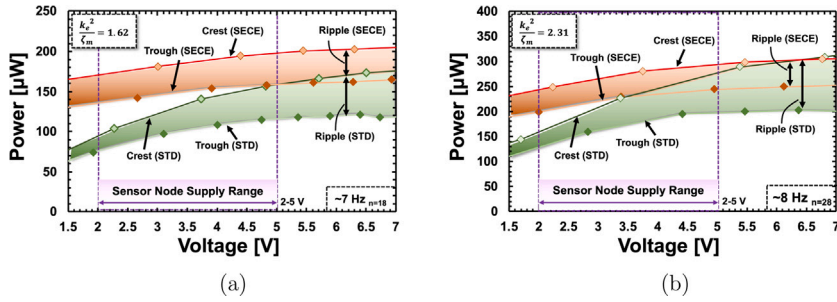
Fig. 13. The measured power envelops of crests and troughs against the output voltage are plotted under various terminal loads ranging from 50 kΩ to 500 kΩ for the SECE (red) and STD (green) interfaces. (a) is the result from the harvester device ($\frac{k_e^2}{\zeta_m} = 1.62$) measured at around 7 Hz. (b) is the result from the harvester ($\frac{k_e^2}{\zeta_m} = 2.31$) measured at around 8 Hz.

$\frac{k_e^2}{\zeta_m} = \frac{\pi}{2}$. The present case with $\frac{k_e^2}{\zeta_m} = 2.31$ deviates from this critical ratio much more than the previous case with $\frac{k_e^2}{\zeta_m} = 1.62$, as seen in Fig. 3(b). Second, the SECE circuit suffices power dissipations mainly due to the incomplete conversion of the energy stored in piezoelectric capacitor and that transferred to the inductor [18,60]. As discussed in Section 5.1, the conversion efficiency of the proposed circuit is measured at around 81%, giving rise to the 20% portion of power reduction from the theoretical estimate shown in Fig. 3(b).

Finally, the smaller mechanical damping ratio results in the enhanced output power up to 350 μW in comparison with the previous case of 200 μW shown in Fig. 11. But it also causes the smaller bandwidth, giving rise to the much steeper ripples in the power frequency of the STD case, as shown in the green curve of Fig. 12(b). Fortunately, the ripples between crests and troughs in the SECE case are much less influenced by the effect of smaller mechanical damping ratio due to the larger electrically induced damping. Indeed, from Eq. (17), Eq. (19) and the parameters listed in the second row of Table 3, ζ_e^{SECE} is 0.035 and ζ_e^{STD} is 0.008. Thus, the operational bandwidth of SECE is significantly improved by slightly increasing the ratio $\frac{k_e^2}{\zeta_m}$ as exemplified by Fig. 4. The consequence of it is the troughs of the power ripples remain at least above 250 μW over the frequency range between 7–12 Hz for the SECE case shown in Fig. 12, giving rise to reliable power supply of sensor nodes against the deviations of driving frequency.

5.3. Sensor-node power supply

One of the applications of the proposed energy harvester device is used to activate sensors for the health monitoring of the rotational instruments. The operational range of the voltage regulator in a sensor node is typically within 2–5 volt. Its equivalent resistance R_{eq} can be estimated by its drain voltage V_{DD} and its required power output P_{supply}

$$R_{\text{eq}} = \frac{V_{\text{DD}}^2}{P_{\text{supply}}}. \tag{29}$$

This load-dependent property could make the STD-based energy harvester not to be operated at the optimal condition, giving rise to the reduction of harvested power. It can be seen from Fig. 3(a) where the electrically induced damping ratio ζ_e^{STD} is strongly dependent on the load resistance while ζ_e^{SECE} is not.

The aforementioned results are crucial in the application of sensor power design. Indeed, Eq. (29) can be replaced by $V_{\text{DD}} = \sqrt{R_{\text{eq}} P_{\text{supply}}}$. Therefore, at the fixed rotary driving frequency around 7 Hz (8 Hz), Fig. 13(a) (Fig. 13(b)) is the power against DC voltage measured by choosing various terminal loads for the SECE and STD cases of the first (second) experimental setup. The red (green) color of shadow region indicates the output fluctuations caused by the crests and troughs of power ripples in the SECE (STD) case. The size of power ripples (the depth of two boundaries between crests and troughs of the power curve) of the SECE case is much smaller than that of the STD case, as particularly exemplified in Fig. 13(b). It is mainly due to $\zeta_e^{\text{SECE}} \gg \zeta_e^{\text{STD}}$ as explained in Fig. 12(b) of Section 5.2. In addition, Fig. 13 shows the shadow regions of red color (SECE) are much flatter than those of green color (STD). It is explained by the SECE property of weak dependence on loads, giving rise to the reliability of power supply based on the SECE conditioning circuit. Finally, Fig. 13 reveals the SECE power output is higher than the STD power output within the typical supply voltage 2–5 volt of a sensor node. But unlike the results from Fig. 11(b) and Fig. 12(b) where the STD output power is evaluated at the optimal load, the STD power against the DC voltage in Fig. 13 exhibits the load dependence based on Eq. (29). As a result, the difference of power output between SECE and STD are observed to be much wider in Fig. 13 than in Fig. 11(b) and Fig. 12(b), especially at the lower voltage ranging from 2–3 volt.

6. Conclusions

The article investigates the electrical response of an SECE-based piezoelectric frequency up-converted energy harvester operated under rotary magnetic plucking. Specifically, the harvester device consists of a piezoelectric beam with a tip magnet impulsively

excited by another magnet fixed on a rotating plate. A consequence of it is that an initially high output voltage is continuously damped and oscillatory within the time interval between two adjacent events of pluckings, giving rise to the inefficient extraction of power. Such a drawback is overcome by the proposed SP-SECE circuit consisting of a MOS switch for enlarging the range of working voltage and a voltage divider for minimizing the switching delay effect.

A theoretical model for realizing the phenomenon of frequency up-conversion is established based on the Fourier decomposition of magnetic impulsive force. It shows that the device is under the resonant excitation whenever the driving rotary frequency is equal to the device's resonant frequency divided by certain integer. In addition, the analytic SECE power output is explicitly derived, as in Eq. (6), for estimating peak power and its fluctuations observed in rotary power frequency response. It raises an issue of the competition between high power and low ripples. This motivates the introduction of an electrically induced damping ratio ζ_e^{SECE}, and the results inferred from it are listed below.

(a). First, $\zeta_e^{\mathrm{SECE}} \approx \frac{k_e^2}{\frac{\pi}{2}}$ and is independent of load resistance where k_e^2 is the electromechanical coupling factor;

(b). The impedance matching for achieving the optimal power requires $\frac{k_e^2}{\zeta_m} = \frac{\pi}{2}$ where ζ_m is the mechanical damping ratio;

(c). If $\frac{k_e^2}{\zeta_m} > \frac{\pi}{2}$, then $\zeta_e^{\mathrm{SECE}} > \zeta_m$. The consequence of it is the enlargement of the half-power bandwidth by Eq. (21) at the cost of power decrement.

(d). Eq. (20) shows that ζ_e^{SECE} is at least 4 times larger than ζ_e^{STD} which is the electrically induced damping ratio of the case based on the standard (STD) interface circuit. This combined with (c) gives the power fluctuations in SECE much more reduced than STD.

The SECE rotary power frequency response is experimentally investigated and compared with the analytic prediction in two proposed experiments with different ratios of $\frac{k_e^2}{\zeta_m}$. First, the results shown in Fig. 11(a) and Fig. 12(a) conclude the theoretical predictions based on Eq. (6) agree well with the experimental observations, giving rise to the soundness of the proposed model suitable for the performance evaluation of an SECE-based frequency up-converted harvester. In addition, Fig. 11(b) with $\frac{k_e^2}{\zeta_m} = 1.62$ close to the SECE impedance matching value $\frac{\pi}{2}$ shows the SECE power outperforms the STD power. This observation is consistent with the prediction (b) mentioned above. Further, Fig. 12(b) comes from another experiment with $\frac{k_e^2}{\zeta_m} = 2.31$. It exhibits the much more pronounced reduction of power ripples observed in the SECE case than in the STD case, as predicted by the arguments of (c) and (d) above. Finally, the properties of load-independence and low ripples make the SECE-based frequency up-converted harvester superior in powering sensor nodes. Indeed, Fig. 13 confirms the stable power supply from SECE operated at the output voltage of a sensor node between 2–5 volt.

Declaration of competing interest

The authors declare that they have no known competing financial interests or personal relationships that could have appeared to influence the work reported in this paper.

Acknowledgments

References

[1] C. Wei, X. Jing, A comprehensive review on vibration energy harvesting: Modelling and realization, Renew. Sustain. Energy Rev. 74 (2017) 1–18.

[2] N. Wu, B. Bao, Q. Wang, Review on engineering structural designs for efficient piezoelectric energy harvesting to obtain high power output, Eng. Struct. 235 (2021) 112068.

[3] A. Erturk, D.J. Inman, Piezoelectric Energy Harvesting, Wiley, 2011.

[4] M.F. Lumentut, I.M. Howard, Analytical and experimental comparisons of electromechanical vibration response of a piezoelectric bimorph beam for power harvesting, Mech. Syst. Signal Process. 36 (2013) 66–86.

[5] W.C. Tai, L. Zuo, On optimization of energy harvesting from base-excited vibration, J. Sound Vib. 411 (2017) 47–59.

[6] Y.C. Shu, I.C. Lien, Efficiency of energy conversion for a piezoelectric power harvesting system, J. Micromech. Microeng. 16 (2006) 2429–2438.

[7] N. Aboulfotoh, J. Twiefel, On developing an optimal design procedure for a bimorph piezoelectric cantilever energy harvester under a predefined volume, Mech. Syst. Signal Process. 106 (2018) 1–12.

[8] W. Zhou, B. Wang, C.W. Lim, Z. Yang, A distributed-parameter electromechanical coupling model for a segmented arc-shaped piezoelectric energy harvester, Mech. Syst. Signal Process. 146 (2021) 107005.

[9] Y. Liao, H. Sodano, Optimal power, power limit and damping of vibration based piezoelectric power harvesters, Smart Mater. Struct. 27 (2018) 075057.

[10] G. Clementi, M. Ouhabaz, S. Margueron, M.A. Suarez, F. Bassignot, L. Gauthier-Manuel, D. Belharet, B. Dulmet, A. Bartasyte, Highly coupled and low frequency vibrational energy harvester using lithium niobate on silicon, Appl. Phys. Lett. 119 (2021) 013904.

[11] S. Sukumaran, S. Chatbouri, D. Rouxel, E. Tisserand, F. Thiebaud, T.B. Zineb, Recent advances in flexible PVDF based piezoelectric polymer devices for energy harvesting applications, J. Intell. Mater. Syst. Struct. 32 (2021) 746–780.

[12] D. Guyomar, A. Badel, E. Lefeuvre, C. Richard, Toward energy harvesting using active materials and conversion improvement by nonlinear processing, IEEE Trans. Ultrason. Ferroelectr. Freq. Control 52 (2005) 584–595.

[13] M. Lallart, D. Guyomar, An optimized self-powered switching circuit for non-linear energy harvesting with low voltage output, Smart Mater. Struct. 17 (2008) 035030.

[14] X. Wang, X. Liang, Z. Hao, H. Du, N. Zhang, M. Qian, Comparison of electromagnetic and piezoelectric vibration energy harvesters with different interface circuits, Mech. Syst. Signal Process. 72-73 (2016) 906–924.

[15] M. Lallart, S.R. Anton, D.J. Inman, Frequency self-tuning scheme for broadband vibration energy harvesting, J. Intell. Mater. Syst. Struct. 21 (2010) 897–906.

[16] Z. Li, Z. Yang, H.E. Naguib, Introducing revolute joints into piezoelectric energy harvesters, Energy 192 (2020) 116604.

[17] Z. Wang, Y. Du, T. Li, Z. Yan, T. Tan, A flute-inspired broadband piezoelectric vibration energy harvesting device with mechanical intelligent design, Appl. Energy 303 (2021) 117577.

[18] P.H. Wu, J.T. Lin, Y.C. Lo, Y.C. Shu, An SECE array of piezoelectric energy harvesting, Smart Mater. Struct. 30 (2021) 045008.

[19] Y. Zhang, K. Bian, Y. Gu, M. Ye, W. Tian, W. Liu, Cost-effective and scalable rectifier design for multiple piezoelectric power sources with improved performance, J. Intell. Mater. Syst. Struct. 31 (2020) 167–181.

[20] S. Fang, G. Miao, K. Chen, J. Xing, S. Zhou, Z. Yang, W.H. Liao, Broadband energy harvester for low-frequency rotations utilizing centrifugal softening piezoelectric beam array, Energy 241 (2022) 122833.

[21] R.M. Toyabur, M. Salauddin, H. Cho, J.Y. Park, A multimodal hybrid energy harvester based on piezoelectric electromagnetic mechanisms for low-frequency ambient vibrations, Energy Convers. Manage. 168 (2018) 454–466.

[22] X. Li, D. Upadrashta, K. Yu, Y. Yang, Analytical modeling and validation of multi-mode piezoelectric energy harvester, Mech. Syst. Signal Process. 124 (2019) 613–631.

[23] Z. Wang, T. Li, Y. Du, Z. Yan, T. Tan, Nonlinear broadband piezoelectric vibration energy harvesting enhanced by inter-well modulation, Energy Convers. Manage. 246 (2021) 114661.

[24] S. Zhou, J. Cao, D.J. Inman, J. Lin, D. Li, Broadband tristable energy harvester: Modeling and experiment verification, Appl. Energy 133 (2014) 33–39.

[25] F. Qian, M.R. Hajj, L. Zuo, Bio-inspired bi-stable piezoelectric harvester for broadband vibration energy harvesting, Energy Convers. Manage. 222 (2020) 113174.

[26] M.M. Ahmad, N.M. Khan, F.U. Khan, Review of frequency up-conversion vibration energy harvesters using impact and plucking mechanism, Int. J. Energy Res. 45 (2021) 15609–15645.

[27] R. Dauksevicius, R. Gaidys, V. Ostasevicius, R. Lockhart, A.V. Quintero, N. de Rooij, D. Briand, Nonlinear piezoelectric vibration energy harvester with frequency-tuned impacting resonators for improving broadband performance at low frequencies, Smart Mater. Struct. 28 (2019) 025025.

[28] M. Pozzi, M. Zhu, Plucked piezoelectric bimorphs for knee-joint energy harvesting: Modelling and experimental validation, Smart Mater. Struct. 20 (2011) 055007.

[29] X. Rui, Y. Zhang, Z. Zeng, G. Yue, X. Huang, J. Li, Design and analysis of a broadband three-beam impact piezoelectric energy harvester for low-frequency rotational motion, Mech. Syst. Signal Process. 149 (2021) 107307.

[30] B. Kathpalia, D. Tan, I. Stern, A. Erturk, An experimentally validated model for geometrically nonlinear plucking-based frequency up-conversion in energy harvesting, Smart Mater. Struct. 27 (2018) 015024.

[31] Y. Kuang, Z. Yang, M. Zhu, Design and characterisation of a piezoelectric knee-joint energy harvester with frequency up-conversion through magnetic plucking, Smart Mater. Struct. 25 (2016) 085029.

[32] T. Xue, S. Roundy, On magnetic plucking configurations for frequency up-converting mechanical energy harvesters, Sensors Actuators A 253 (2017) 101–111.

[33] Y.C. Shu, I.C. Lien, Analysis of power output for piezoelectric energy harvesting systems, Smart Mater. Struct. 15 (2006) 1499–1512.

[34] E. Lefeuvre, A. Badel, C. Richard, D. Guyomar, Piezoelectric energy harvesting device optimization by synchronous electric charge extraction, J. Intell. Mater. Syst. Struct. 16 (2005) 865–876.

[35] J. Liu, J. Yang, R. Han, Q. He, D. Xu, X. Li, Improved interface circuit for enhancing the power output of a vibration-threshold-triggered piezoelectric energy harvester, Energies 13 (2020) 3830.

[36] A. Morel, A. Quelen, P. Gasnier, R. Grezaud, S. Monfray, A. Badel, G. Pillonnet, A shock-optimized SECE integrated circuit, IEEE J. Solid-State Circuits 53 (2018) 3420–3433.

[37] H. Fu, E.M. Yeatman, Effective piezoelectric energy harvesting using beam plucking and a synchronized switch harvesting circuit, Smart Mater. Struct. 27 (2018) 084003.

[38] H. Fu, E.M. Yeatman, Rotational energy harvesting using bi-stability and frequency up-conversion for low-power sensing applications: Theoretical modelling and experimental validation, Mech. Syst. Signal Process. 125 (2019) 229–244.

[39] H. Fu, X. Mei, D. Yurchenko, S. Zhou, S. Theodossiades, K. Nakano, E.M. Yeatman, Rotational energy harvesting for self-powered sensing, Joule 5 (2021) 1074–1118.

[40] Y.H. Fu, Micro Piezoelectric Energy Harvester Applied in Broadband Rotational Energy Harvesting System. MS. Thesis, National Taiwan Univesity, 2018.

[41] H.G. Yeo, T. Xue, S. Roundy, X. Ma, C. Rahn, S. Trolier-McKinstry, Strongly (001) oriented bimorph PZT film on metal foils grown by rf-sputtering for Wrist-Worn piezoelectric energy harvesters, Adv. Funct. Mater. 28 (2018) 1801327.

[42] P. Pillatsch, E.M. Yeatman, A.S. Holmes, A piezoelectric frequency up-converting energy harvester with rotating proof mass for human body applications, Sensors Actuators A 206 (2014) 178–185.

[43] Y.C. Lo, T.Y. Yeh, Y.C. Shu, Sece-based piezoelectric energy sensor for the diagnostics of timing belt, Proc. SPIE 12043, 2022, pp. 273–281, http://dx.doi.org/10.1117/12.2612277.

[44] H. Fu, E.M. Yeatman, A methodology for low-speed broadband rotational energy harvesting using piezoelectric transduction and frequency up-conversion, Energy 125 (2017) 152–161.

[45] Y.C. Shu, W.C. Wang, Y.P. Chang, Electrically rectified piezoelectric energy harvesting induced by rotary magnetic plucking, Smart Mater. Struct. 27 (2018) 125006.

[46] Y.C. Lo, C.C. Chen, Y.C. Shu, M.F. Lumentut, Broadband piezoelectric energy harvesting induced by mixed resonant modes under magnetic plucking, Smart Mater. Struct. 30 (2021) 105026.

[47] C. Jettanasen, P. Songsukthawan, A. Ngaopitakkul, Development of micro-mobility based on piezoelectric energy harvesting for smart city applications, Sustainability 12 (2020) 2933.

[48] C.L. Kuo, S.C. Lin, W.J. Wu, Fabrication and performance evaluation of a metal-based bimorph piezoelectric MEMS generator for vibration energy harvesting, Smart Mater. Struct. 25 (2016) 105016.

[49] X. Wang, Y. Xia, G. Shi, H. Xia, Y. Ye, Z. Chen, Self-powered piezoelectric and thermoelectric energy simultaneous extraction interface circuit based on double stack resonance, IEEE Trans. Ind. Electron. 67 (2020) 4567–4577.

[50] L. Zhu, R. Chen, X. Liu, Theoretical analyses of the electronic breaker switching method for nonlinear energy harvesting interfaces, J. Intell. Mater. Syst. Struct. 23 (2012) 441–451.

[51] Y. Wu, A. Badel, F. Formosa, W. Liu, A.E. Agbossou, Self-powered optimized synchronous electric charge extraction circuit for piezoelectric energy harvesting, J. Intell. Mater. Syst. Struct. 25 (2014) 2165–2176.

[52] W. Liu, C. Zhao, A. Badel, F. Formoas, Q. Zhu, G. Hu, Compact self-powered synchronous energy extraction circuit design with enhanced performance, Smart Mater. Struct. 27 (2018) 047001.

[53] G. Shi, Y. Xia, Y. Ye, L. Qian, Q. Li, An efficient self-powered synchronous electric charge extraction interface circuit for piezoelectric energy harvesting systems, J. Intell. Mater. Syst. Struct. 27 (2016) 2160–2178.

[54] M. Lallart, E. Lefeuvre, C. Richard, D. Guyomar, Self-powered circuit for broadband, multimodal piezoelectric vibration control, Sensors Actuators A 143 (2008) 377–382.

[55] L. Zhao, L. Tang, Y. Yang, Synchronized charge extraction in galloping piezoelectric energy harvesting, J. Intell. Mater. Syst. Struct. 27 (2016) 453–468.

[56] E. Lefeuvre, A. Badel, C. Richard, D. Guyomar, Energy harvesting using piezoelectric materials: Case of random vibrations, J. Electroceram. 19 (2007) 349–355.

[57] L. Tang, Y. Yang, Analysis of synchronized charge extraction for piezoelectric energy harvesting, Smart Mater. Struct. 20 (2011) 085022.

[58] G.A. Papagiannopoulos, G.D. Hatzigeorgiou, On the use of the half-power bandwidth method to estimate damping in building structures, Soil Dyn. Earthq. Eng. 31 (2011) 1075–1079.

[59] Z. Chen, J. He, J. Liu, Y. Xiong, Switching delay in self-powered nonlinear piezoelectric vibration energy harvesting circuit: Mechanisms, effects and solutions, IEEE Trans. Power Electron. 34 (2019) 2427–2440.

[60] C. Chen, B. Zhao, J. Liang, Revisit of synchronized electric charge extraction (SECE) in piezoelectric energy harvesting by using impedance modeling, Smart Mater. Struct. 28 (2019) 105053.